Characterization of laser plasmas for interaction studies

L. A. Gizzi,[1] D. Giulietti,[2] A. Giulietti,[1] T. Afshar-Rad,[3] V. Biancalana,[1] P. Chessa,[1]
C. Danson,[4] E. Schifano,[5] S. M. Viana,[3] and O. Willi[3]
[1]*Istituto di Fisica Atomica e Molecolare via del Giardino, 7-56127 Pisa, Italy*
[2]*Dipartimento di Fisica, Università di Pisa, Pisa, Italy*
[3]*The Blackett Laboratory, Imperial College of Science, Technology, and Medicine, London, United Kingdom*
[4]*Central Laser Facility, Rutherford Appleton Laboratory, Chilton, Didcot, United Kingdom*
[5]*Laboratoire pour l'Utilisation des Lasers Intenses, Ecole Polytechnique, Palaiseau, France*
(Received 31 January 1994)

Long scale length plasmas were produced by uniform laser irradiation from opposite sides of metal disks coated on thin plastic stripe targets. The plasma became fully underdense before the end of the 600-ps pulse. The evolution of the plasma was carefully characterized both in electron density and temperature, and the experimental data were compared to the predictions of a one-dimensional hydrodynamics computer code. The electron temperature was obtained from time-resolved x-ray spectra by line-ratio measurements, accounting for opacity effects. Two-dimensional electron density profiles of a large plasma region were obtained by Nomarski interferometry at different times. They showed that the expansion was axially symmetric and reproducible shot by shot. The plasma was found to be substantially free from small-scale density inhomogeneities. The plasma produced with this techique is very suitable for interaction experiments. In particular, laser stimulated plasma instabilities of relevance for laser fusion can be accurately studied in these conditions.

PACS number(s): 52.50.Jm, 52.40.Db, 52.70.−m, 07.60.−j

I. INTRODUCTION

The interaction of laser light with the underdense plasma surrounding the spherical capsule in the "direct-drive" inertial confinement fusion (ICF) scheme is of crucial concern as it plays a key role in determining the degree of uniformity of pellet compression. In fact, filamentation instability (FI) and self-focusing (SF) can occur in this region which can enhance laser intensity nonuniformities and consequently affect the uniformity of the ablation pressure. On the other hand, several detrimental laser-driven plasma instabilities, including stimulated Brillouin scattering (SBS), stimulated Raman scattering, and two-plasmon decay, can be efficiently activated by a local increase of intensity subsequent to the onset of FI and/or SF. Consequently the study of the physics of laser interaction with large underdense plasmas is of fundamental significance for the achievement of the control and eventually the suppression of these instabilities. To this purpose several different experimental schemes have been considered and tested so far.

Here we only consider the experimental approach consisting in the production of underdense plasmas by laser heating of thin targets (exploding foil plasmas [1]) and the eventual interaction of this preformed plasma with a suitably delayed laser pulse [2]. Plasmas produced from exploding foils also proved to be adequate as amplifying media for x-ray lasers [3]. The combined effort, in the past few years, of laser-plasma interaction studies and x-ray laser research has resulted in the developing of a variety of techniques for the production and characterization of exploding foil plasmas. Analytical [4,5] models have been developed that allow the hydrodynamic expansion of such plasmas to be described. Numerical codes are presently in use worldwide that can provide simulations of the plasma temporal evolution from both an hydrodynamic as well as an atomic physics viewpoint. Only recently, however, more attention has been devoted to a systematic experimental characterization of these plasmas which could provide, on one side, a satisfactory knowledge of plasma conditions for the analysis of interaction experiments and, on the other side, an adequate test bed for analytical and numerical models of plasma hydrodynamics and atomic physics.

In one of the typical configurations to produce exploding foil plasmas, which is relevant to both interaction studies and x-ray laser experiments, known as line-focus geometry, the target consists of a metal stripe coated onto a very thin plastic substrate. This is a preferential way of producing long scale length plasmas. In this configuration the interaction beam propagates along the length of the stripe; this length is chosen according to the desired plasma scale length which, in the case of interaction experiments, is of the order of 1 mm. An alternative target for the line-focus configuration consisted of a free standing H-shaped foil directly supported by the target holder. The preformed plasmas obtained from either coated stripe targets or "H targets" were characterized [6] in terms of electron density uniformity. It was found that with stripe targets the denser and colder plasma generated from the plastic (Formvar) substrate can significantly perturb the metal plasma, limiting its expansion and eventually giving rise to density nonuniformities over the whole target extent. This effect, combined with the small transverse density scale length, can seriously

perturb the propagation of the interaction beam in the plasma. Nonuniformities were found to be reduced by using H targets, which, on the other hand, are more difficult to manufacture [6]. Density nonuniformities as well as detrimental consequences of the Formvar plasma can also be reduced by optimizing the aspect ratio of the coated stripe and using wider line-focus laser spots. A number of interaction experiments [7–10] have been performed with optimized targets in the line-focus configuration. An essential feature of this configuration is that the plasma expands transversally to the interaction beam, thus virtually eliminating Doppler shift and broadening from the spectra of the light scattered either forward or backward. This condition, though not realistic with respect to ICF coronal plasmas, allows one to gain "cleaner" information on some instabilities. In particular, SBS spectral components appeared unusually clear in this configuration [7].

In another category of experimental arrangements the interaction beam propagates perpendicularly to the target plane, i.e., parallel to the flow velocity of the preformed expanding plasma. Heating laser beams are typically focused on target into circular spots. In this configuration, also known as cylindrical geometry, a thin dot target is used whose diameter defines the transverse density scale length while the longitudinal scale length is set by the hydrodynamics of plasma expansion. In contrast to the line-focus configuration, in the cylindrical geometry the interaction beam propagates in an expanding plasma with high flow velocities. This fact can strongly affect the spectra of scattered radiation. For example, assuming a plasma completely underdense at the time of interaction, the effect of the flow velocity on the spectra can be used to study the interaction of laser light with the expanding corona of a fusion pellet, provided that the interaction is limited to the portion of the plasma expanding toward the laser.

Recently, particular attention has been devoted [11] to study interaction physics in a cylindrical geometry with plasmas at high electron temperatures (≥ 1 keV) and therefore in conditions closer to those of a typical ICF corona. In this regime, due to the low efficiency of inverse bremsstrahlung absorption, the interaction beam is expected to cause a minimal perturbation to the plasma hydrodynamics. The high temperature plasma was preformed developing a method [12,13] previously used on extended plastic foils. Dot plastic targets were irradiated [14] with a sequence of two or three sets of beams staggered in time. In that experiment the plasma temperature was evaluated from time-resolved x-ray spectroscopy of K-shell Al emission from Al doped plastic targets. The density was estimated from stimulated Raman spectra. Additional information on the evolution of the electron density was obtained from a simple Schlieren technique which was also compared with an advanced two-dimensional hydrodynamic simulation.

Nevertheless for a greater relevance of experimental investigation to the physics of laser-driven plasma instabilities, it is important to operate in a regime where a stronger interaction occurs between the laser light and the plasma. Plasma electron densities of special interest to ICF coronal studies typically range from hundredths to tenths of the critical density. Sub-KeV plasmas with a density scale length of fractions of millimeter provide favorable conditions for interaction experiments in a strongly perturbed regime. In this regime the physics of laser induced instabilities including flow effects can be better understood than in conditions more "realistic" for ICF.

Our experiment was designed to accomplish these conditions using a configuration simplified with respect to that of Refs. [13] and [14] to generate a plasma less hot but more reactive to the interaction with a delayed beam. The preformed plasma was created by symmetric irradiation of thin Al dots placed in the near field of the four heating beams with the heating beam spots considerably larger than the dot itself. This choice allowed the irradiation to be particularly uniform on target. The distribution of the electron density was measured at different delays by interferometry with a short probe pulse. Time-resolved x-ray spectroscopy provided line intensity ratios for measurements of electron temperature. After a few nanoseconds, the preformed plasma had a long scale length density profile with a peak density well below the critical density. At that time the temperature was uniform and of the order of several hundreds of eV.

The experiment was designed in order to meet suitable conditions in view of a systematic investigation [15] of the filamentation instability and stimulated Brillouin scattering. In particular, the experiment investigated the effect of spatial laser intensity gradients on laser-plasma interaction dynamics. Intensity modulations were induced in the far field of the interaction beam using specially designed [16] plates with a controlled phase. This paper is mainly concerned with the characterization of plasma conditions while the work on the interaction physics will be presented in forthcoming publications. One of the aims of this work is to prove that the plasmas produced with this method are suitable for a wide class of experiments on the laser-plasma interaction.

The experimental setup for the production of large underdense plasmas is described in Sec. II along with the diagnostic devices used for plasma characterization. Section III is devoted to the measurements of the electron density distribution as obtained from the analysis of interferometric patterns. The limits of this technique are also discussed and the method used to extract the phase shift map from the fringe pattern is introduced. A few basic equations related to the analysis of interferogram are reported in the Appendix. The sensitivity of our interferometer to small scale density perturbations is evaluated in Sec. III, where second harmonic generation is also considered as a test of plasma uniformity. Section IV deals with time-resolved x-ray spectra used to measure the electron temperature and its evolution. Plasma opacity is taken into account and the results of numerical stimulation of x-ray line intensity ratios are presented. In Sec. V both density and temperature measurements are discussed and compared with the predictions of one-dimensional (1D) hydrodynamic simulation. Advantages and limits of plasma production using ir laser light are also discussed. Conclusions are drawn in Sec. VI.

II. EXPERIMENTAL SETUP

The experiment described here was performed at the Science and Engineering Research Council (SERC) Central Laser Facility, United Kingdom. The main features of the experimental setup are shown in the layout of Fig. 1. Four 600-ps 1.0530-μm beams of the Vulcan laser were used to preform the plasma. The four beams were lying in the same vertical plane. These *heating* beams were focused with $f/10$ optics and superimposed on target in two opposed pairs in a 600-μm-diam spot, which provided a total intensity up to 1.2×10^{14} W/cm^2 (up to 6.0×10^{13} W/cm^2 on each side). Each pair was composed of two beams at angles of $+13°$ and $-13°$ to the normal to the target plane, respectively. As discussed in Sec. V, the intensity was limited to the value given above to avoid undesired nonlinear effects in the plasma formation. Targets consisted of 0.5-μm-thick 400-μm-diam aluminum dots coated onto a 0.1-μm plastic stripe support, whose width was also about 400 μm. The four heating beams were superimposed and the target was placed 6 mm ahead of the focal plane of each beam in the center of the spot. Since the focal depth of each beam was approximately 1 mm, the target was basically located in the near field of these beams. Typical near field intensity nonuniformities had a scale length of one-twentieth of beam size and were limited to 20% of the average intensity. The estimated accuracy in the positioning of the target relatively to the beams and of the beams relatively to each other was better than 50 μm. The energy balance of the four beams was typically better than 10%; data obtained with a larger energy misbalance have not been taken in account. The relative timing of the four heating pulses on target was accurate within a few tens of picoseconds. The overall experimental accuracy resulted in a highly reproducible plasma over more than 100 laser shots.

The 600-ps 1.053-μm interaction beam was delayed by 1–3.5 ns with respect to the heating pulses and focused with an $f/15$ optics into the preformed plasma along the main symmetry axis of the exploded target, at an intensity ranging from 10^{13} to 5×10^{14} W/cm^2. The focal spot diameter was typically 100 μm, i.e., much smaller than the plasma transverse scale length, to avoid refraction effect at the plasma boundary. Other focusing conditions were also adopted including line focus induced by lens tilting and phase plate manipulation.

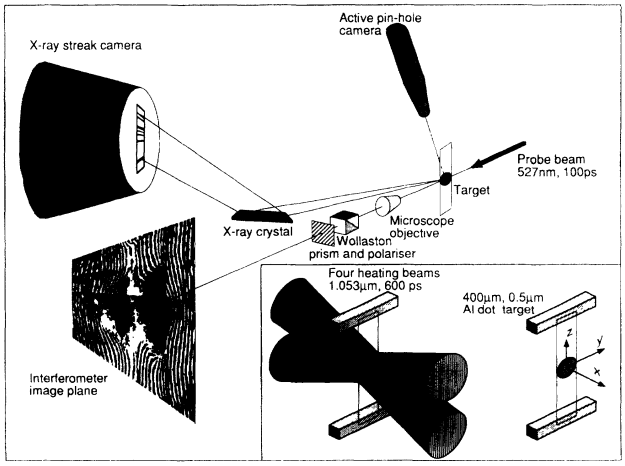

FIG. 1. Experimental setup for the production and characterization of long scale length expanding plasmas for ICF coronal studies. In the separate frame enclosed in the figure also represented are the Al dot target, the plastic substrate and the target holder (right), and the configuration of the four heating beams on target.

A sixth 100-ps [full width at half maximum (FWHM)] beam was frequency doubled to 0.53 μm, delayed, and used as a probe beam for interferometric measurements in a line of view parallel to the target plane (see Fig. 1). A modified Nomarski interferometer [17–19] was employed in order to measure electron density profiles. It basically consists of a polarized light interferometer which produces, by means of a Wollaston prism, two separate orthogonally polarized images of the plasma surrounded by an unperturbed background. Interference between each of the two images and the background of the other image is achieved by a polarizer, put before the film plane, oriented at 45° with respect to the two polarization axes.

It should be noted that since a frequency doubled probe beam was used, sources of second harmonic generated (SH) by the laser beams could also be imaged at 90° with respect to the x-z plane (see Fig. 1). Actually a narrow-band interference filter at the SH wavelength was placed in front of the film to reject unwanted plasma self-emission and scattering at other wavelengths, thus making it possible to obtain time-integrated SH images. The spatial resolution of these images was measured to be better than 10 μm in the object plane.

An x-ray spectrometer consisting of a flat thallium hydrogen phthalate (TlAP) crystal ($2d=25.9$ Å) was set in a first-order Bragg configuration, in order to spectrally resolve x-ray radiation emitted from the plasma. An intensified x-ray streak camera fitted with a CsI photocathode was coupled to the spectrometer. A spectral region from approximately 5.4 to 7.0 Å was selected in order to study resonance line emission from He-like and H-like aluminum. The temporal resolution was given by the fixed slit in front of the streak camera cathode and was, depending on the selected streak speed, 50 ps for some spectra and 100 ps for some others, as specified below. The spectral resolution, basically set by the size of the emitting region, was evaluated directly from calibrated x-ray spectra and was found to be typically 40 mÅ. This value is in agreement with a simple calculation made by assuming a plasma emitting region whose size is given by the projection of Al dot target on a plane perpendicular to the line of sight of the spectrometer. This evaluation is also supported by time-integrated x-ray images obtained using an active pin-hole camera set symmetrically to the streak camera with respect to the interaction beam. In fact, these images show that the x-ray emitting region matches the Al dot.

III. INTERFEROMETRY AND DENSITY MEASUREMENTS

Electron density profiles of the preformed plasma have been obtained via interferometric measurements using a

short-pulse optical probing technique in a Nomarski interferometric configuration, as described in the preceding section. Very recently a work has been published [20] where a grid image refractometry technique was successfully used to obtain two-dimensional density profiles of a test plasma, simply produced by single beam irradiation of a thick target. In that paper the advantages of this technique are considered in comparison with some other refractometry techniques, including the Schlieren method. The authors of that paper also consider the limits of the interferometric techniques for large size plasmas and complain of the scarcity of published 2D experimental density profiles of laser plasmas.

A general discussion on interferometric studies of laser plasmas is beyond the scope of the present paper. In this section 2D electron density profiles of a plasma region of considerable extent are shown. They were obtained from high quality interferograms with a method presented in some detail, including phase shift mapping and Abel inversion. Several aspects related to the fringe pattern formation and visibility are discussed, and small scale sensitivity is evaluated. The lack of evidence for the second harmonic generated in the plasma by the heating beams, in contrast with the strong generation produced by the interaction beam, is finally presented as further proof of the preformed plasma homogeneity.

A. Fringe pattern and visibility

Interferograms of the plasma were taken at various delays relative to the peak of the heating pulses in order to monitor the temporal evolution of the electron density. We found that, under analogous intensity conditions, interferograms were highly reproducible shot by shot. In the following, in order to support some preliminary estimates, we will anticipate some results of 1D hydrodynamic simulation. A full account of this simulation will be reported on in Sec. V.

In the analysis of the interferograms we will assume that the plasma electron density is much smaller than the critical density for the probe wavelength (as confirmed by the data analysis) and that density gradients allow the probe beam to propagate through the whole plasma without undergoing severe bending. A simple estimate of the validity of this last assumption, which is also the most restrictive one, can be obtained in the approximation of a cylindrical plasma with a parabolic density profile, in which case the maximum angular deflection is given by the peak electron density divided by the critical density. The phase disruption induced by bending effects on the probe is negligible provided [21] that $n_e/n_{c@0.5\mu m} \ll \alpha$, where n_e is the peak electron density, $n_{c@0.5\mu m}$ is the critical electron density at the wavelength of the probe beam, and α is the acceptance angle of the interferometer. According to the simulation, 2.0 ns after the peak of the heating pulses the peak density on the target plane is 1.7×10^{20} cm^{-3}, which gives $n_e/n_{c@0.5\mu m} < 0.12\alpha$. Therefore, under the conditions of interest for interferometric measurements, namely, for times after the heating pulses greater than 2 ns, refraction effects are not expected to significantly perturb the probe beam.

Two representative interferograms are analyzed here that were obtained at approximately the same heating irradiance and with the interaction beam turned off. The interferogram of Fig. 2(a) was taken 4.3 ns after the peak of the heating pulses which was the earliest time at which fringes were visible over the whole plasma extent. At earlier times there was a lack of fringes in the region around the plasma density peak as shown in the next interferogram. The total heating intensity was 8.5×10^{13} W/cm^2. Figure 2(a) shows part of the interferometric pattern consisting in one of the two fringe systems as described in Sec. II. The fringes on the extreme left-hand

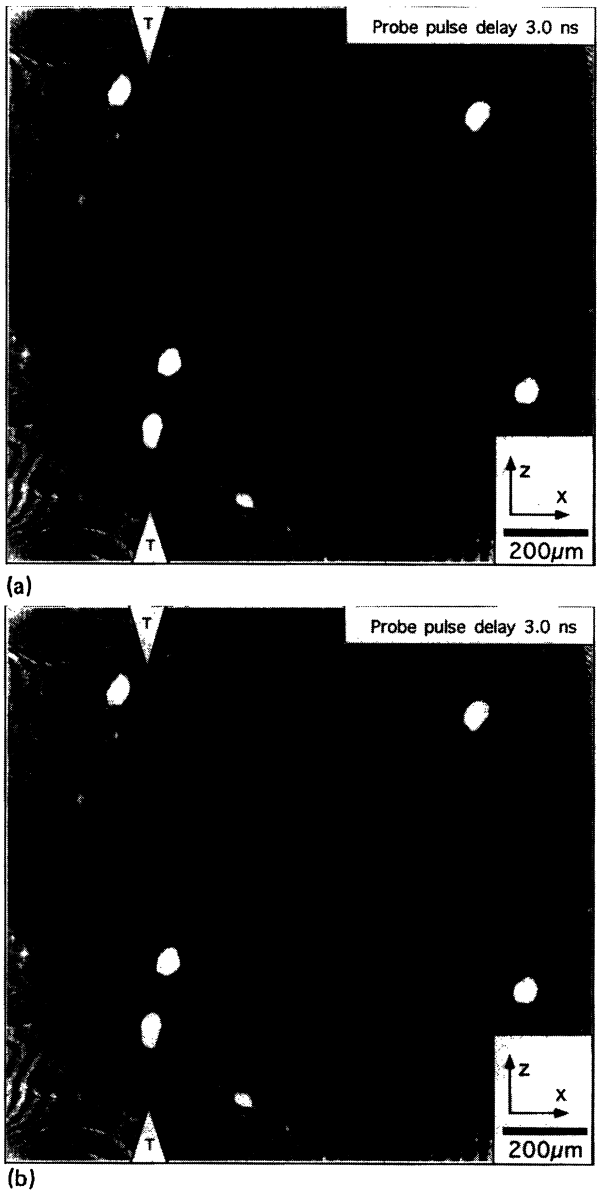

FIG. 2. (a) Interferogram of the preformed plasma taken 4.3 ns after the peak of the heating laser pulses. The intensity on target was 8.5×10^{13} W/cm^2. The probe pulse length was 100 ps and the probe wavelength was 0.53 μm. The original target position is shown by the arrows labeled with a T. (b) Interferogram of the preformed plasma taken 3.0 ns after the peak of the heating laser pulses. The intensity on target was 6.0×10^{13} W/cm^2. Other features are the same as in (a).

side of the image are perturbed due to the overlapping with the other fringe system. The original position of the target is marked by two arrows and the target holder expansions are visible on the top left and bottom left of the image. Moreover, a minor fraction of the energy in the wing of the focal spot of the heating beams hits the holder, producing a tenuous plasma giving rise to a local perturbation of the fringe pattern. The plasma created from the plastic substrate is also expected to slightly contribute to the fringe pattern in the region close to the original target position.

The interferogram of Fig. 2(b) was taken 3.0 ns after the peak of the heating pulses, at a heating intensity of 6.5×10^{13} W/cm^2. The white spots visible on the image are due to imperfections of the film. As pointed out above in this section, the fringe visibility vanishes in the denser region of the plasma at this probe delay. As already shown above, bending effects cannot account for this loss of fringe visibility. Absorption of the probe beam energy has also been taken into account, assuming propagation of the beam in a density profile obtained from the simulation at 3.0 ns. It has been found to be typically less than 10% of the probe energy. Therefore absorption is expected to have a marginal effect on the fringe visibility. The main contribution to the depletion of fringe visibility, observed in Fig. 2(b) in the denser central plasma region, comes from the electron density evolution which smears out part of the pattern during the probe pulse duration. In fact, according to simulations, 3 ns after the peak of the heating pulses, the electron density in this region decreases at a rate of 3×10^{19} cm^{-3} ns^{-1}. Therefore, during the 100-ps probe pulse, this rate gives a density variation of typically 3×10^{18} cm^{-3}. This variation, integrated over a 400-μm path, leads to a phase change of $\Delta\varphi=2.5$ rad, which can, by itself, account for the observed loss of visibility. This effect vanishes at later times as the rate of density change decreases. For example, 4.3 ns after the peak of heating pulses, according to the simulation, the rate drops to less than one-third of that predicted at 3.0 ns, giving a fringe shift of one-fourth of a fringe separation. This is consistent with the interferogram of Fig. 2(a), which shows fringes up to the center of the plasma. Nevertheless, as expected, the visibility is found to decrease towards the center.

B. Phase shift measurements

The phase shift distribution as function of x and z coordinates has been extracted from the interferograms, employing a fringe analysis technique [22] based on Fourier transform method. Such technique has been successfully applied [23] to the analysis of interferograms of laser-produced plasmas and has proved to be extremely powerful. In fact, it allows the information carried by the fringe position on the film to be decoupled from the spatial variations of the background intensity as well as by variations in the fringe visibility, provided that the scale length of such perturbations is large compared to the fringe separation.

The phase shift induced by the plasma is experimentally detected measuring the displacement of the fringes from their unperturbed position. The intensity of the fringe pattern on the film in the presence of the plasma can be written as [22]

$$I(x,z)=a(x,z)+[c(x,z)\exp(2\pi i f_u x)+\text{c.c.}]\,. \quad (1)$$

In this equation $c(x,z)=\frac{1}{2}b(x,z)\exp[i\Delta\varphi(x,z)]$ and its complex conjugate $c^*(x,z)$ contains all the information relative to the phase shift $\Delta\varphi(x,z)$ induced by the plasma; $a(x,z)$ and $b(x,z)$ account for nonuniformities of the background intensity and the fringe visibility respectively and f_u is the spatial frequency of the unperturbed fringe pattern, i.e., the number of fringes per unit length on the film [see also Eq. (A1) in the Appendix]. The Fourier transform of the fringe pattern intensity of the interferogram of Fig. 2(a) was calculated for different z-axis positions. The modulus of this transform is shown in Fig. 3 (top) as a grey-scale image. Some details of this calcula-

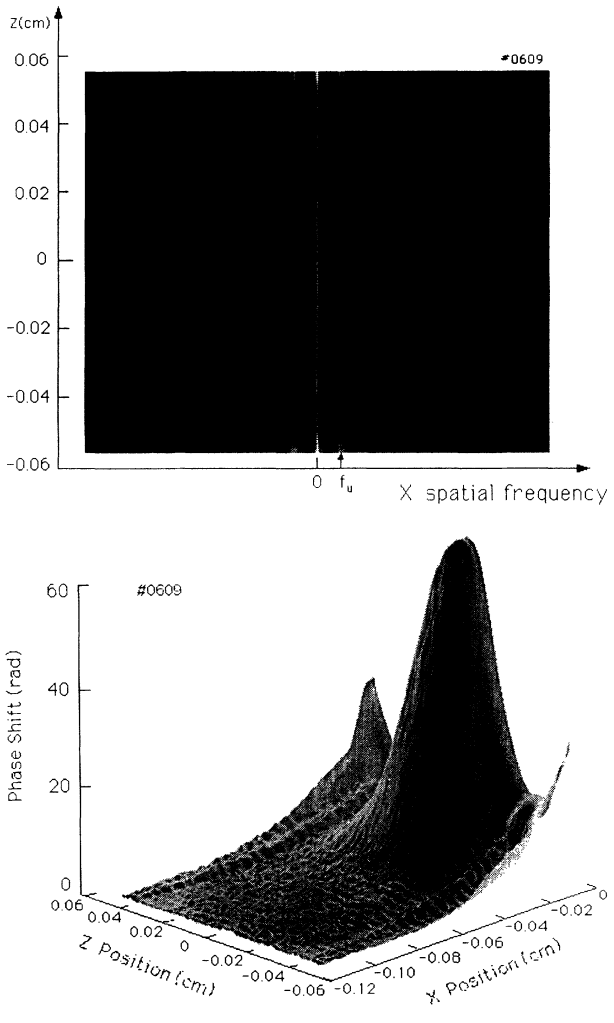

FIG. 3. Top: fast Fourier transform (FFT) of the intensity profile of the interferogram of Fig. 2(a). The FFT was performed along the x axis, perpendicular to the unperturbed fringes. The natural logarithm of the modulus of the FFT is shown as a grey-scale image. Bottom: 3D shaded surface of the phase shift distribution as obtained from the interferogram of Fig. 2(a) using a Fourier transform based technique (see text).

tion are given by Eqs. (A4) and (A5) in the Appendix. The sidebands (symmetric to the *zero* frequency) are relative to the fringe pattern, while the strong central component accounts for the background. Figure 3 (bottom) shows a 3D shaded surface of the phase distribution relative to the interferogram of Fig. 2(a) as obtained from the frequency spectrum shown in Fig. 3 (top) (see the Appendix for details).

Figure 4(a) shows a contour plot of the phase shift distribution of Fig. 3 (bottom) with a contour interval of π. Contour lines are highly symmetric with respect to the x axis in the x-z plane. This validates the assumption of cylindrical symmetry of the plasma around the x axis.

The same technique was employed to analyze the interferogram of Fig. 2(b). A contour plot of the phase shift distribution obtained from that interferogram is shown in Fig. 4(b), where contour levels are labeled in radians. The shaded area denotes the region of the interferogram where the phase shift could not be determined, the fringe visibility in this region being below the detection level.

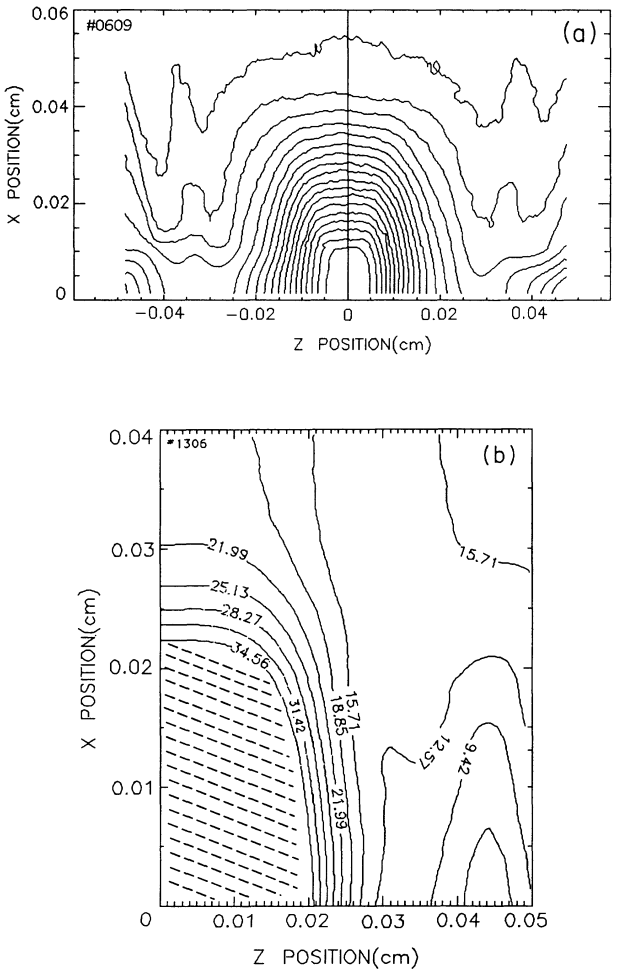

FIG. 4. (a) Contour plot of the phase shift relative to the interferogram of Fig. 2(a) taken 4.3 ns after the peak of the heating pulses. (b) Contour plot of the phase shift relative to the interferogram of Fig. 2(b) taken 3.0 ns after the peak of the heating pulses.

C. Two-dimensional electron density profiles

According to Eq. (A3) in the Appendix, the phase distributions of Figs. 4(a) and 4(b) have been used to determine the electron density distribution. The integral has been solved numerically using a corrected composite trapezoid rule. Due to the large amount of phase data points available, typically 512×512, the integral could be performed, in most cases, directly on the data itself, without polynomial fitting. On the other hand, when such procedure was necessary, as in the case of data affected by high level of spatial frequency noise, the high sampling frequency of the phase distribution ensured that no uncertainty was introduced by the particular choice of curve fitting.

Figure 5(a) shows a contour plot of the electron density

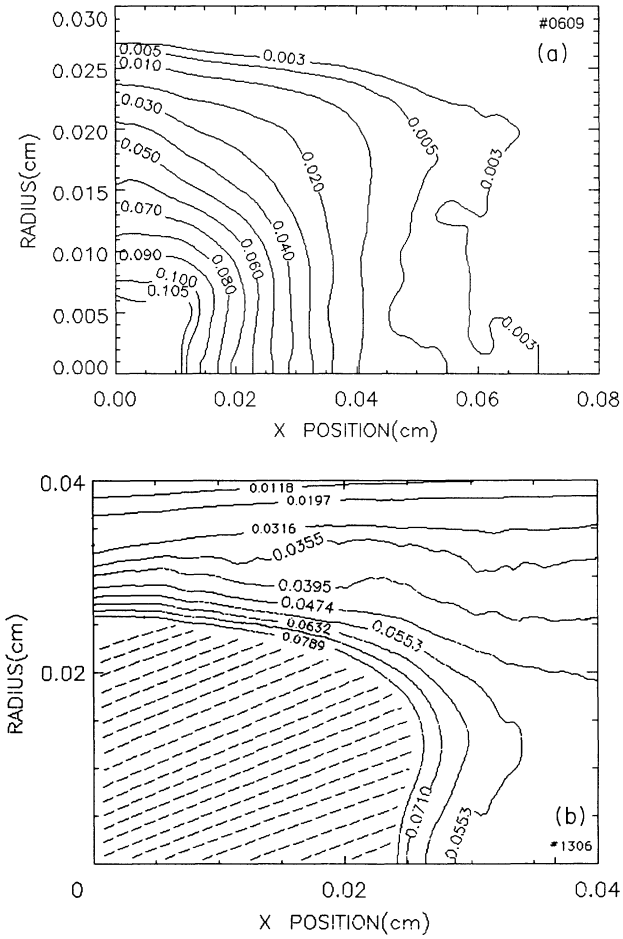

FIG. 5. (a) Contour plot of the electron density profile of the preformed plasma at 4.3 ns after the peak of the heating pulses. Contour levels are labeled in units of the critical density at 1.053 μm. The electron density distribution of the preformed plasma was obtained performing Abel inversion of the phase shift distribution of Fig. 4(a). (b) Contour plot of the electron density profile of the preformed plasma at 3.0 ns after the peak of the heating pulses. Contour levels are labeled in units of the critical density at 1.053 μm. The electron density distribution of the preformed plasma was obtained performing Abel inversion of the phase shift distribution of Fig. 4(b).

profile 4.3 ns after the peak of the heating pulses, as extracted from the interferogram of Fig. 2(a). The contour levels are labeled in units of the critical density for a 1.053-μm laser wavelength. Notice that in Figs. 5(a) and 5(b), the z coordinate used in Fig. 4 has been replaced by the *radial* coordinate, as a consequence of the assumed cylindrical symmetry. The contribution to the phase shift due to the plasma blowoff from the edges of the target holder was eliminated by multiplying the phase shift by an appropriate function:

$$\Delta\varphi(x,z) \Longrightarrow \Delta\varphi(x,z)\exp[-(z/w_z)^{2n}] \ . \tag{2}$$

w_z and n were chosen in order to achieve a smooth cutoff of the unwanted contribution without appreciably modifying the phase shift due to the main plasma. Although this procedure introduced some arbitrariness in the phase distribution of the marginal regions, the density profiles obtained from Abel inversion were found to be rather insensitive to the particular choice of the values given to w_z and n.

Figure 5(b) shows a contour plot of the electron density profile at 3.0 ns after the peak of the heating pulses, relative to the interferogram of Fig. 2(b) obtained by Abel inversion of the phase shift distribution of Fig. 4(b). We observe that the dense plasma region extends along the x axis over a distance of the order of the original aluminum dot diameter, while a lower density (a few times 10^{18} cm^{-3}) plasma extends over a 1-mm-sized region. The density profile at 3.0 ns is a more important reference for the interaction measurements performed mostly 2.5 ns after the plasma production.

The electron density profiles shown in this section will be discussed in Sec. V in terms of the suitability of the preformed plasma for interaction experiment. These profiles will be also compared with 1D simulation data and a possible failure of the cylindrical approximation close to the original target position will be considered.

D. Small-scale uniformity

Small-scale perturbations of the preformed plasma are an important feature of the plasma *quality*. In fact, they can affect laser-plasma interaction and modify the condition of growth of the particular instability under study. It is therefore relevant to estimate the sensitivity of the interferometric technique to small-scale density perturbations and consequently assess the degree of homogeneity of the plasma.

According to Eq. (A1) and in the approximation of Eq. (A2) in the Appendix, the phase shift induced by the plasma has a linear dependence upon the electron density. The contribution of a local electron density inhomogeneity to the total phase shift can therefore be written as

$$\delta\varphi(x,z) = -\frac{\pi}{\lambda_p n_{c@0.5\,\mu m}} \int_{-L/2}^{L/2} \delta n_e(x,y,z)dy \ , \tag{3}$$

where $\delta n_e(x,y,z)$ is the density inhomogeneity. In other words, the phase shift induced by a density fluctuation is independent from the background electron density. We evaluated $\delta\varphi$ at a given position (x_0,z_0) on the output plane of the interferometer, assuming a density inhomogeneity along the line of sight given by $\delta n_e(x_0,y,z_0) = a n_{c@1\,\mu m}\exp(-y^2/w^2)$, where a and w are the amplitude of the density perturbation in units of the critical density $n_{c@1\,\mu m}$ and its scale length, respectively. Figure 6 shows a contour plot of $N=\delta\varphi(0,0)/2\pi$ as a function of the two parameters a and w with the contour levels labeled in units of the number of fringe shifts. The range of the perturbation scale length considered in Fig. 6 is of particular relevance to laser driven instabilities in coronal plasmas. The use of the Fourier technique for interferogram analysis allows a very accurate determination of the phase shift distribution. An estimate of the limit of this accuracy can be made from the contour plots of Figs. 4(a) and4(b) and it is basically set by the small-scale noise which affects the position of the contour curves. This effect leads to an uncertainty of the order of typically 0.5 rad. Consequently, a single perturbation along the line of sight with a small scale length of 20 μm will be detected as long as the corresponding amplitude of density fluctuation is greater than $0.01 n_{c@1\,\mu m}$. This limit becomes $0.025 n_{c@1\,\mu m}$ for a 10-μm scale length perturbation. This conclusion makes the interferometer used in this work able to detect plasma inhomogeneity distinctive of most of the instabilities relevant to ICF presently under investigation.

The interferograms of the plasmas obtained in this experiment generally showed a good small-scale homogeneity as shown by the two examples of Figs. 5(a) and 5(b). Notice that the lowest density contour lines show spatial modulations that are, according to the previous evaluations, out of the spectrometer sensitivity and consequently with no clear physical meaning. We found, however, important deviations from local homogeneity during the delayed interaction of those plasmas with manipulated interaction beams.

E. Second harmonic emission

As already pointed out in Sec. II, the interferometer allows SH radiation emitted sidewards by the plasma to be

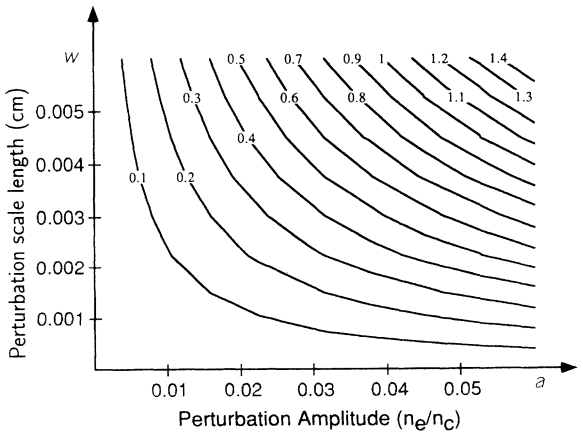

FIG. 6. Contour plot of the phase shift (in number of fringe shifts) induced by a Gaussian perturbation in the electron density along the line of sight of the interferometer as a function of the transverse perturbation scale length w and the perturbation amplitude a in units of the critical density at 1.053 μm.

imaged out. SH emission can take place during the heating of the plasma and eventually during the interaction of the delayed pulse with the underdense plasma. SH emission sideward can occur in the presence of the critical layer due to the nonlinear mixing of electron plasma waves (at the same frequency as the incident laser light) with laser photons or with other plasma waves at the same frequency. A number of mechanisms, including resonance absorption and parametric decay instability, can account for the production of these electron plasma waves close to the critical density layer. On the other hand, SH side emission can also originate [24] from underdense plasmas in the presence of density gradients perpendicular to the incident laser light. This mechanism makes SH emission an important diagnostic tool to monitor the degree of uniformity of the plasma and in particular the onset of filamentation instability.

SH emission generated by the interaction beam in the underdense plasma has indeed been detected by the interferometer. Figure 7(a) shows an interferogram of the plasma taken 2 ns after the peak of the heating pulse. The total heating intensity was 9.4×10^{13} W/cm^2. The interaction pulse was timed to reach the plasma 1.5 ns after the peak of the heating pulse. The interaction beam was focused on the plasma in a line focus with the longitudinal axis set along the line of view of the interferometer. The focal spot was approximately 800 μm long and 100 μm wide and the average intensity was approximately 1.2×10^{14} W/cm^2. Both fringe patterns of the plasma produced by the interferometer are displayed in Fig. 7(a). SH emission is produced by the interaction beam as it propagates through the plasma. SH is localized at the boundaries of the main bulk of the plasma. One can observe that the SH emitted at the output boundary is less intense, probably due to absorption of the interaction beam energy by the plasma. It is very relevant to notice that no SH sources were detected when the interaction beam was switched off, as shown, for example, in the interferograms of Figs. 2(a) and 2(b).

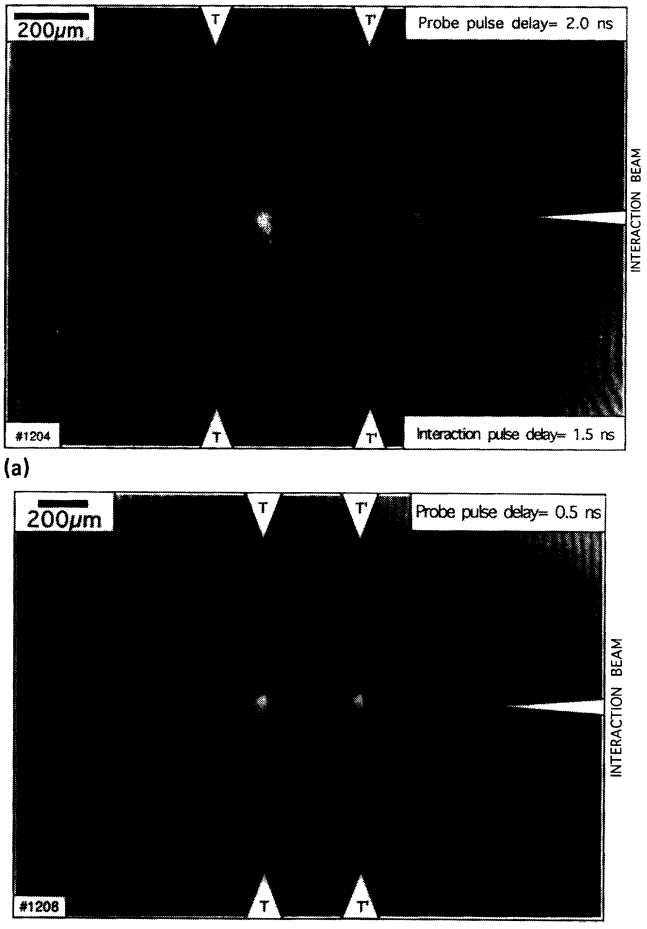

FIG. 7. (a) Interferogram of the preformed plasma taken 2.0 ns after the peak of the heating pulses showing the SH emitted by the interaction beam (heating to interaction delay: 1.5 ns). The total heating intensity was 9.4×10^{13} W/cm^2 while the interaction intensity was 1.2×10^{13} W/cm^2. (b) Interferogram of the plasma produced by a localized heating of the dot aluminum target showing strong SH emission in proximity of the target surface. Probe pulse delay 0.5 ns.

On the other hand, strong SH emission was also observed when the heating was localized to a small portion of the target. Figure 7(b) shows an interferogram obtained with the heating pulses turned off. The beam usually devoted to the delayed interaction was set to heat the Al dot target directly with the same line focusing described above, at an average laser intensity of 1.0×10^{14} W/cm^2. The probe pulse was delayed by 500 ps with respect to the main pulse. The strong SH emission occurring in proximity of the target surface suggests that the intensity nonuniformities introduced by the focal spot boundaries and the consequent formation of density gradients in the plasma play a dominant role in the production of SH emission.

From the observations in Figs. 7(a) and 7(b) we can conclude that, when conditions are suitable for SH generation, strong SH emission is indeed detected. The absence of observable SH emission during the plasma formation by the heating beams provides a clear indication of the high level of uniformity of the plasma produced.

IV. X-RAY EMISSION AND TEMPERATURE MEASUREMENTS

The analysis of the x-ray spectra has been carried out considering the dependence of line radiation from He-like and H-like Al ions on the electron temperature. The comparison of measured line ratios with the predictions of the steady state atomic physics numerical computer code RATION [25] for a given temperature and density allows electron temperature to be estimated [26]. Opacity effects have been included in the calculation and evaluated for different lengths of homogeneous plasma. In order to minimize the uncertainty in the determination of electron temperature due to opacity effects we have restricted the analysis to the high quantum number members of each resonance series. On the other hand, the intensity of the resonance lines decreases dramatically going toward high quantum number members, resulting in poor signal-to-noise ratios. The intensity ratio between the aluminum Ly-γ and He γ lines has been considered here as it represents, in our experimental conditions, the

best compromise between these two limits. It will be shown that, although opacity effects in general play an important role in determining the intensity of x-ray emission lines emerging from the plasma, at the time at which plasma conditions are of interest for interaction experiments they lead to a small error in the final value of electron temperature.

A. Time-resolved x-ray spectra

Figure 8(a) shows a typical time-resolved spectrum, obtained in the same shot as the interferogram of Fig. 2(a). Figure 8(b) shows a 1D trace taken 500 ps after the peak of the Heβ line emission and integrated over 50 ps, which is also the temporal resolution of the spectrum. Emission lines from the Heβ to the Ly-δ are clearly visible with the Ly-γ and Ly-δ emerging from the He-like continuum. Line intensity profiles were found to be well fitted by a Gaussian profile with $\Delta\lambda_{\mathrm{FWHM}}=40$ mÅ$\pm$10%. All the lines, except the Heε and Lyβ, are well resolved by allowing a direct evaluation of the line intensity. With the available spectral resolution (set by the source extent) the Lyβ line is only partially resolved being merged with the Heε and higher quantum number He-like lines and with the He-like continuum edge.

The time-resolved spectrum shown in Fig. 9(a) was obtained in similar conditions as in Fig. 8(a), but with a heating laser intensity of 1.2×10^{14} W/cm^2 and with the interaction pulse reaching the plasma 2.5 ns after the peak of heating pulses. The temporal resolution was 100 ps in this spectrum. Compared to the spectrum of Fig. 8(a), the Ly-γ and Ly-δ lines now clearly emerge from the He-like continuum as an effect of the higher temperature, due to the higher intensity of the heating beams. This circumstance make x-ray spectra like this, obtained at higher laser intensities, more suitable for temperature measurements from line intensity ratios between H-like and He-like lines. The electron temperature obtained in these conditions can be reliably extended to lower heating laser intensities comparing experimental data with numerical simulation.

The Ly-γ to Heγ intensity ratio of the spectrum of Fig. 9(a), restricted to the heating phase only, is shown in Fig. 9(b). The portion of the spectrum of Fig. 9(a) produced during the delayed interaction with the underdense plasma will be analyzed in detail in a forthcoming paper devoted to the interaction physics. We simply notice here that the spectral resolution is apparently improved for this part of the spectrum due to the smaller extent of

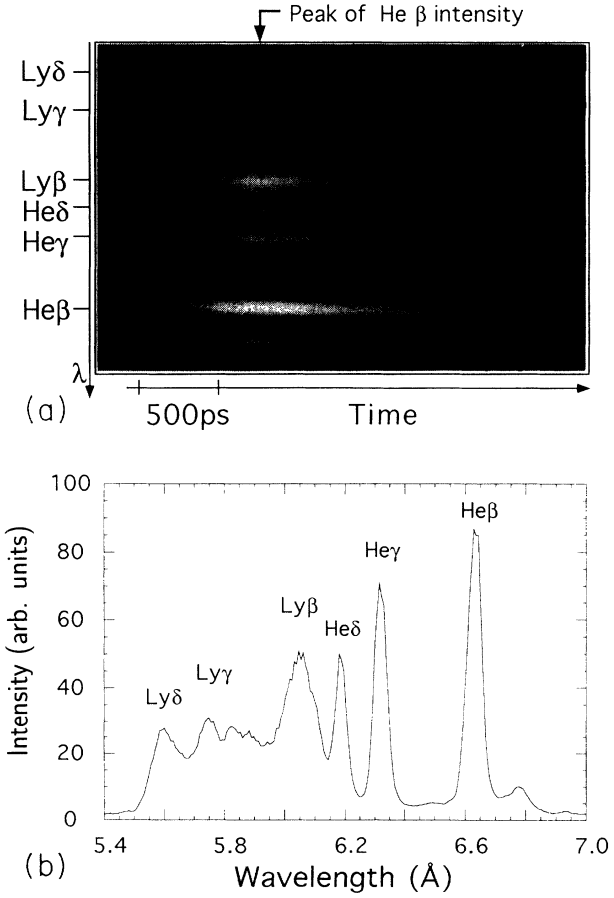

FIG. 8. (a) Time-resolved x-ray spectrum of K-shell Al emission from plasma produced at a heating intensity of 6×10^{13} W/cm^2. (b) Line out of the spectrum of (a) taken 500 ps after the peak of Heβ line intensity and integrated over 50 ps, which is the temporal resolution of the spectrum.

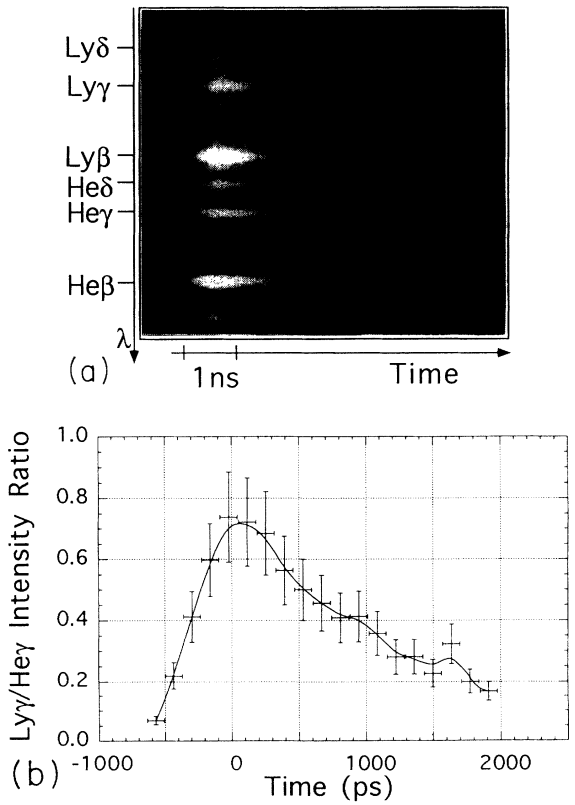

FIG. 9. (a) Time-resolved x-ray spectrum of K-shell Al emission from plasma produced at a heating intensity of 1.2×10^{14} W/cm^2. In this case the interaction beam was delayed by 2.5 ns with respect to the peak of the heating pulses. (b) Experimental intensity ratio of the H-like Al γ line ($1s$-$4p$) to the He-like Al γ line ($1s^2$-$1s4p$) as a function of time relative to the peak emission.

the focal spot of the interaction beam with respect to the target size. Furthermore there is evidence for a rather surprising shift (variable in time) of the spectral lines. This effect must be chiefly due to the motion of the intense part of the x-ray source during the interaction pulse.

B. Temporal evolution of electron temperature

As already pointed out, our spectra resulted from spatial integration integrated over the whole plasma extent. Consequently plasma parameters determined by the analysis of line emission spectra should, in principle, be regarded as averaged over the whole plasma. However, since line emission intensity originating from a given ion species is strongly dependent on the local electron temperature and density, we can expect that particular plasma regions will give dominant contribution to the line emission. An estimate of such an effect has been made in the approximation of coronal equilibrium, in an optically thin steady state plasma. Such an approximation is likely to be unrealistic at the beginning of the heating pulse, when the density of the emitting plasma is too high and laser intensity increases too rapidly for a steady state, thin plasma model to hold. However, later in time, typically after the peak of the heating laser pulses, the electron temperature is high enough and the electron density low enough for the conditions of the coronal equilibrium to be fulfilled. The intensity of the line emission relative to a transition from a level n to the ground state of a given ion depends upon density and temperature according to

$$I_{n\to 0} \propto n_e n_0 T_e^{-1/2} \exp(-\Delta E_{n\to 0}/T_e) , \tag{4}$$

$\Delta E_{n\to 0}$ being the transition energy and n_0 the ground state population density of the given ion species. If we assume that most ions are in their ground state, then $n_0 \approx n_i$. For a given ion charge Z, $I_{n\to 0}$ is a function of the hydrodynamic plasma parameters T_e and n_e.

Equation (4) has been evaluated as a function of time, post-processing the results of the numerical simulation performed using the 1D Lagrangian hydrodynamics code MEDUSA [27,28] for the typical heating conditions of our experiment. In the code the laser energy is absorbed by the plasma via inverse bremsstrahlung absorption and resonance absorption. Thermal conductivity is modeled in terms of the classical Spitzer-Härm conductivity [29], with the electron thermal flux limited, for large temperature gradients, to a fraction of the free-streaming limit [30]. Input parameters can be specified which include laser irradiation features, i.e., wavelength, intensity, and pulse shape. Finally the spatially dependent population densities of the ground state of each ionization stage is calculated in nonlocal thermal equilibrium (NLTE). Typically between 90% and 99% of the ions are in their ground state; consequently a minor error arises from this assumption when the average ionization degree is calculated from the ground state population densities of the ions.

A single side irradiation configuration was considered by fixing the target boundary opposed to the laser and by halving the target thickness and the laser intensity.

In order to evaluate the contribution of the thin plastic substrate to the hydrodynamic evolution of plasma, numerical simulation of the laser irradiated Al targets with and without the CH layer was carried out. In the first case a two-layer (CH-Al) target consisting of 0.1 μm CH and 0.25 μm Al was set to be irradiated on the CH side at an intensity of 3×10^{13} W/cm^2. The electron temperature and density profiles obtained in this condition were compared with analogous profiles obtained considering a 0.25-μm-thick Al layer without plastic. According to the simulation, the presence of the CH layer affects the main Al plasma only slightly, the main consequence being that a plasma is produced which is slightly colder than in the case of irradiation of Al without CH. This is essentially due to the fact that, early in the heating pulse, interaction takes place in the low Z plasma originating from the plastic layer where collisional absorption is much less efficient. In particular, at 2 ns after the peak of the heating pulse, the electron temperature is found to be 550 eV in the presence of the CH layer and 640 eV with no CH layer. As a consequence of the lower electron temperature, the plasma expands slightly less and the peak density is approximately 20% higher than in the case of irradiation without a CH layer. We can conclude that the CH layer gives rise to minor differences in the electron density and temperatures profiles on the two sides of the target plane. So far as interaction experiments are concerned, the interaction beam is always injected in the plasma from the side originating from the bare Al. We will consequently focus our attention on this side of the plasma.

The electron temperature and density profiles and the ion density profile of the ion species of interest, i.e., He-like ions, have been determined by the simulation and used to calculate the emissivity of the Heβ line. We found that as long as the plasma is still overdense, the emissivity increases going towards the higher electron density regions and reaches its maximum in proximity of the critical density layer. Going further towards the supercritical density region, the emissivity decreases rapidly as a consequence of the lower local electron temperature. Similar features can be observed later in time when most of the x-ray line emission comes from a narrow region whose temperature and density maximize the emissivity as given by Eq. (4). Figure 10(a) shows the calculated intensity of the Heβ line, integrated over the whole plasma, as function of time with respect to the peak of the heating laser pulse. According to the simulations the x-ray emission reaches its peak approximately 100 ps after the peak of the heating laser pulse. The result of the simulation is compared with the experimental intensity of the Heβ line obtained from the spectrum of Fig. 8(a). The discrepancy between experimental and theoretical data early during the emission is a consequence of the assumption of the steady state coronal model which, as explained above, cannot properly describe this stage of the plasma. More significant is the slower rate of emission decay observed experimentally, if compared with theory. This discrepancy was already observed in a previous research [31], where time-resolved spectra from a laser plasma were compared with a code using a heat flux limiter of 0.1, the

same value we used for the simulation of Fig. 10(a). The analysis of this effect requires a more sophisticated modeling of x-ray emission processes, which is presently in progress.

Further insight into the dynamics of the x-ray emission is provided by the plots of Fig. 10(b), which show the temporal behavior of the Heβ peak emissivity and the electron density at which such peak takes place. As long as the plasma is overdense, i.e., initially in the laser pulse, the peak of emission is located in a plasma region with electron density between n_c and $3n_c$. Once the maximum plasma density has fallen below the critical value, the laser propagates through the plasma and heats it more uniformly. Consequently a dominant contribution to the x-ray line emission will come from the region of maximum electron density located in proximity of the original target position.

The simulated Ly-γ to Heγ intensity ratio has been plotted in Fig. 11(a) as a function of plasma electron density, at two different electron temperatures with opacity effects included in the calculation. Three different opacity conditions have been considered for each value of the electron temperature. At densities below a few times 10^{19} cm^{-3} the intensity ratio is almost independent of both density and opacity effects. However, in the range of electron densities of our interest, i.e., between a few times 10^{19} cm^{-3} and a few times 10^{21} cm^{-3}, there is a strong dependence of the line ratio upon the electron density. In addition we observe that opacity strongly affects line ratios only at electron densities above 10^{20} cm^{-3}. Therefore during the plasma generation, density and opacity are expected to play a dominant role in determining the line intensity ratio. However, later in time, and in particular at the time of interest for interaction experiments, plasma conditions will be such that opacity will affect the Ly-γ to Heγ intensity ratio only slightly. We notice that the region of interest for x-ray line emissivity is always located in proximity of the target plane where plasma hydrodynamics is expected to have a 1D behavior. Therefore the plot of Fig. 10(b), obtained in 1D approximation, can provide the electron density of the x-ray line emitting region necessary to obtain the electron temperature.

Figure 11(b) gives the temporal dependence of electron temperature obtained from the experimental intensity ratio of Fig. 9(b) with the origin of the time axis fixed ac-

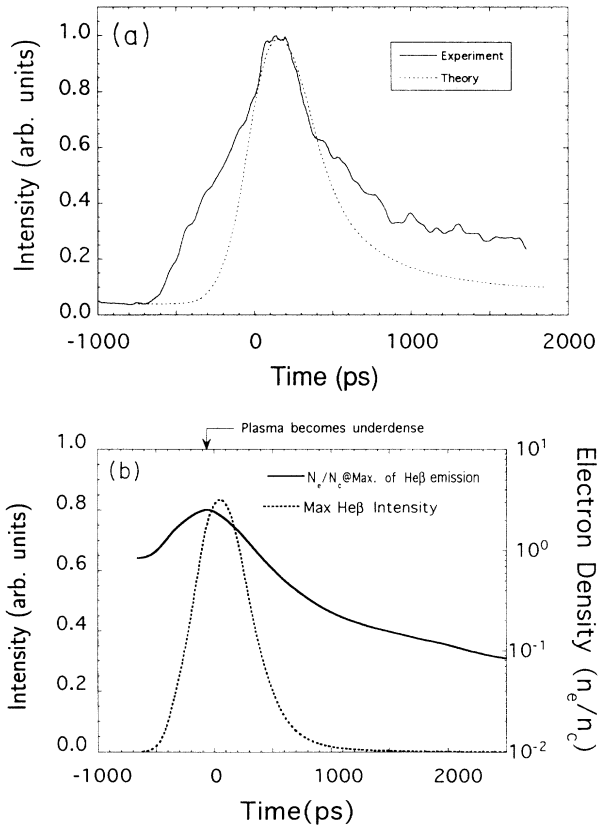

FIG. 10. (a) Calculated intensity of the Heβ line emission integrated over the whole plasma as a function of time with respect to the peak of the heating laser pulse compared with the experimental intensity of Heβ obtained from the spectrum of Fig. 8(a). (b) Calculated temporal behavior of the electron density of the region of plasma where the maximum of Heβ emission is located. In the same graph the temporal behavior of the maximum of the Heβ emission is also plotted. The heating pulse is set to reach its peak at $t=0$ in this graph.

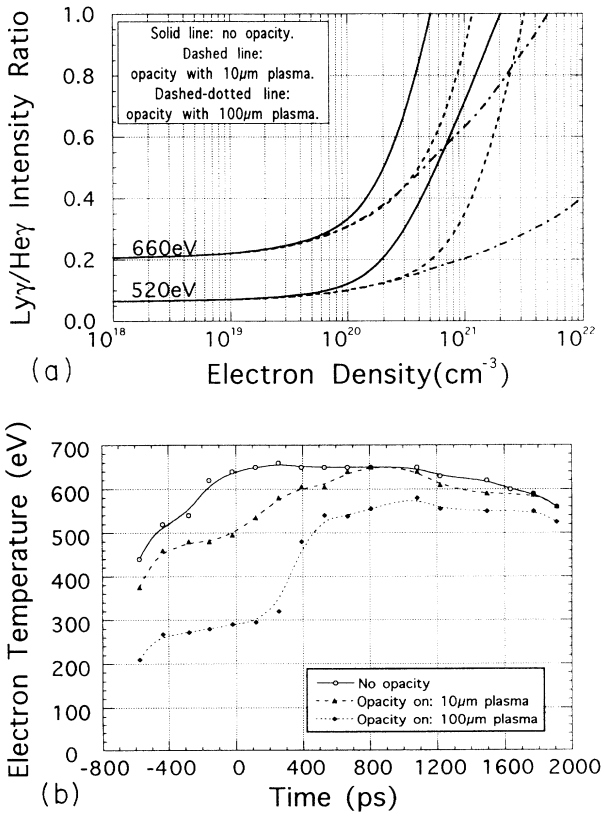

FIG. 11 (a) Calculated Ly-γ to Heγ intensity ratio as function of electron density for different electron temperatures. The solid line has been obtained with no opacity included in the calculation. The dashed line and the dash-dotted line have been obtained with opacity effects included and with the 10- and the 100-μm plasma, respectively. (b) Temporal dependence of the electron temperature obtained assuming the three opacity levels of (a).

cording to the simulation as in the case of Fig. 10(b). As already observed, opacity effects give a dominant contribution during the pulse while later than 0.8 ns after the peak of heating pulses, the three curves tend to give a well defined electron temperature within approximately 100 eV. In particular, at 2 ns, when the peak of the electron density is of the order of one-tenth of critical density, the values of electron temperature obtained from the three curves agree within less than 50 eV, giving an average value of 550 eV (at an intensity of 6×10^{13} W/cm^2 on each side of the target).

V. DISCUSSION

The detailed analysis of interferograms and x-ray spectra gives a comprehensive picture of the plasma created by two-side balanced irradiation of thin Al dot targets. A full system of interference fringes was visible only later than 4 ns after the plasma formation. However, almost complete patterns have been obtained as early as 3 ns and the maximum density can be consistently deduced for earlier times from 1D simulation.

Time-resolved x-ray spectra, appropriately corrected for opacity, can supply the history of the electron temperature. A question arises on where in the plasma most of the x rays used to infer electron temperature are generated. It has been proved in Sec. IV that, at the beginning of the plasma formation, x-ray emission comes from a region close to the critical density. On the other hand, at times of interest for interaction studies, when the plasma is definitely underdense, the temperature is substantially uniform and x-ray emission comes primarily from the plasma region with the highest density. The limit to the x-ray spectral resolution is given by the size of the plasma, which, in the case of interaction studies, has to be rather large both longitudinally and transversally to the plasma flow. In our experiment, however, the line broadening was small enough to allow the electron temperature to be inferred from line intensity ratios.

It is interesting to compare the experimental findings presented so far with the results of the 1D code to realize the main differences between a 1D expansion model and the actual evolution of the plasma. The temperature given by the 1D simulation is almost uniform after the peak of the pulse and is consistent with the measurements obtained in Sec. IV from the time-resolved x-ray spectroscopy. On the contrary, a considerable discrepancy was found between the electron density profiles simulated and those obtained in Sec. III from the interferograms taken at 3.0 and 4.3 ns. In Fig. 12(a) the thicker curves show the experimental electron density profiles along the x axis as obtained 3.0 and 4.3 ns after the plasma formation, respectively. Thinner curves are the theoretical x-axis electron density profiles as resulting from 1D simulation at the same delays. The simulated density decreases very slowly with the distance from the target plane. The experimental curve is solid where the cylindrical approximation is expected to be adequate. The dashed portion of the 4.3-ns experimental curve around the maximum evidences the region where the cylindrical approximation could result in some underestimation of the density (see

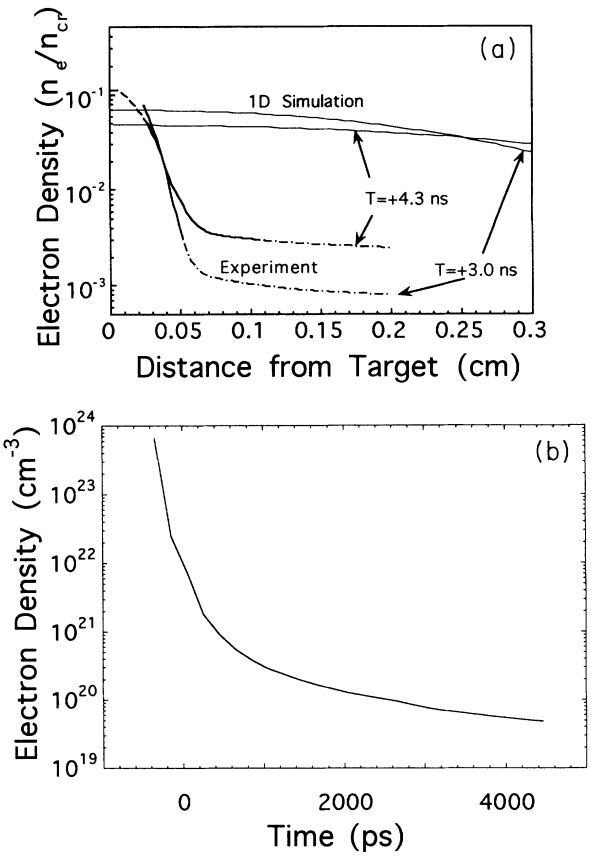

FIG. 12. (a) Comparison between the calculated electron density profiles (1D simulation) and the experimental profiles at 3.0 and 4.3 ns after the peak of the heating pulse, respectively. The dashed and dash-dotted portions of the experimental curves are discussed in the text. (b) Temporal dependence of the maximum electron density as obtained by 1D simulation.

below). The dash-dotted portions of the low density tails were obtained by extrapolation of the experimental density profiles. The experimental electron density is higher than that one obtained from the 1D simulation, in the region close to the original target plane. On the contrary, a much lower density than that in simulation is found at distances of the order of the target diameter from the original target plane. This second discrepancy can be explained by considering that the plasma expansion cannot be described by 1D approximation when the plasma size definitely exceeds the target size.

However, it is rather surprising to find a peak density higher than the one suggested by the 1D expansion. The actual laser energy delivered on target was evaluated very carefully and an overestimation of laser intensity on target can be excluded. We believe that the electron density is overestimated in this region due to a departure of the plasma symmetry from the cylindrical symmetry assumed for the Abel inversion (see Sec. III). In fact, since the spot of the heating beams is larger than the Al dot, a plasma will be produced from the plastic substrate which is mostly at the top and bottom of the dot (see also Fig. 1). These two plasma slabs can confine the aluminum plasma in an elongated shape rather than in a pure cylindrical symmetry, close to the target plane. This

confinement has two consequences: to keep the Al plasma denser than in the case of a free expansion and to elongate the plasma in the line of view of the probe beam (see also Fig. 1). This latter fact will give a phase shift larger than expected in a cylindrical symmetry, thus leading one to overestimate the electron density in the region close to the original target plane. It is therefore assumed that the actual maximum electron density would be not far from the maximum density calculated in the 1D approximation. This assumption can be reasonably extrapolated at shorter times, at which the plasma expansion is closer to 1D and the confining effect of the plastic plasma is much less significant. Figure 12(b) shows the evolution of the maximum electron density in the plasma up to 4.5 ns after the heating pulse, as obtained from the 1D code.

From the point of view of interferometer sensitivity, the deconvolution of the phase distribution obtained from the interferograms gives an accurate mapping of the electron density up to about 1 mm from the original target plane. At larger distances the deconvolution is affected by a considerable error and the density was roughly evaluated independently. The preformed plasma created with our experimental configuration shows a denser, well localized bulk and a lower density tail which 3.0 ns after formation already extends for a few millimeters. These two regions are separated by a rather steep density gradient. Both the gradient and the bulk would prevent the interaction beam from propagating freely in the other side of the plasma. In fact, a calculation shows that 1-μm radiation, propagating in a plasma with a density profile as we observed at 3.0 ns, undergoes very weak absorption in the low density long scale length region, but more than 50% collisional absorption before reaching the density peak. This is a very profitable condition to study interaction phenomena in an underdense long scale length plasma expanding toward the laser. A minor feature is that the density contour lines show a very weak electron density minimum close to the axis. This is likely to be an effect of the slightly higher laser intensity in the center of the spot.

The evaluation of the sensitivity of the interferometer to small scale density nonuniformities as done in Sec. III is a fundamental step for a correct interpretation of interaction experiments. From the point of view of FI, for example, the conclusions drawn in Sec. III indicate that the bulk of the plasma produced with our method is essentially free from those density inhomogeneities able to efficiently initiate the instability. In fact, a few nanoseconds after the plasma formation, when plasma conditions are suitable for interaction experiment, the optimum size for the instability growth is expected [32,33] to be approximately 10–20 μm. On the other hand, the interferograms indicate that the density perturbations of the bulk of the plasma in this range of scale lengths are $\delta n_e / n_e < 0.20$.

These conclusions cannot be extended to the low density plasma blowoff, the amplitude of density inhomogeneities in this region being below the detection level of the interferometer. Nevertheless the plasma in this region will benefit, in terms of homogeneity, from hydrodynamic expansion processes which, at sufficiently large distances from the target plane, should contribute to smooth out residual nonuniformities. On the other hand, from the point of view of laser-driven instabilities, the large density scale length in the direction of propagation of the interaction beam establishes, by itself, favorable condition for instabilities to grow.

It should be stressed here that the use of the fundamental harmonic laser light to preform the plasma, in place of its most commonly used second and third harmonic, has two important advantages. In this case laser intensity nonuniformities are limited to those intrinsic of the laser system described in Sec. II, while harmonic conversion by crystals would considerably enhance intensity nonuniformities. In addition, the use of longer wavelength heating beams results in a larger separation between the critical density layer and the ablation layer during the initial explosion of the target. It has been shown [34] that laser intensity fluctuations at the critical density layer give rise to fluctuations in the thermal electron flux Q at the ablation layer which depend upon perturbation scale length l, average absorbed intensity I_L (in units of 10^{13} W cm^{-2}), and wavelength $\lambda_L(\mu m)$ according to

$$\frac{\Delta Q}{Q} = \exp(-4.5\times 10^{7} I_L^{1/3} \lambda_L^{2/3} t l^{-1}) \frac{\Delta I_L}{I_L} , \tag{5}$$

where t is the time from the beginning of the irradiation in seconds. According to this relation, after 100 ps of laser irradiation at an average absorbed intensity of 10^{13} W cm^{-2}, an intensity perturbation with a scale length of 10 μm gives rise to a perturbation of the same scale length in the electron flux at the ablation layer almost 100 times less intense. In the case of irradiation with fourth harmonic of Nd laser ($\lambda_L = 0.25$ μm), for example, the strength of the perturbation would be reduced only by a factor of 6. In other words, the wavelength of irradiation sets an upper limit to the scale length of perturbation that this process will effectively contribute to smooth out.

Thermal smoothing will also be effective in reducing residual nonuniformities after target explosion; in the typical plasma conditions of our experiment at the end of heating pulses, i.e., at $n_e = 10^{20}$ cm^{-3}, $T_e = 500$ eV, the electron mean free path is typically a few micrometers. Therefore, according to these conclusions, plasma nonuniformities on a scale of less than ≈ 10 μm should also be smoothed out efficiently by thermal conduction before the interaction pulse reaches the plasma a few nanoseconds later. There is recent evidence, however, that, in particular experimental conditions, thermal smoothing is less efficient than expected according to the current models. In fact it was found [35] that when plasmas are generated irradiating solid targets, plasma density inhomogeneities initiated early in the interaction by laser intensity nonuniformities can persist during and after the laser pulse even in presence of laser beam smoothing. Within the limits of sensitivity of the diagnostics employed in our experiment there is no evidence of similar processes occurring in our experimental conditions. In addition, the ir irradiation of the target in our

case has been limited to intensities lower than those typically used for visible or uv light, in order to avoid undesired nonlinear effects which might destroy the plasma homogeneity, as these effects scale roughly as $I_L\lambda_L^2$. In the case of a 1-μm wavelength and according to the typical intensity thresholds of the main nonlinear processes active in the laser-plasma interaction, an intensity of 10^{14} W/cm^2 can be regarded as a cautious limit below which no major disturbances to the plasma from such mechanisms can be expected. For this reason the heating intensity on each side of the target was kept below this limit. This conclusion is strongly supported by the experimental results described in this work.

VI. CONCLUSION

The method of symmetrical laser irradiation of thin metal disks, coated on very thin plastic stripes, has been proved to be very effective in producing plasmas suitable for interaction studies. The choice of ir beams at moderate intensity for plasma formation purposes was successful in terms of plasma density homogeneity. The geometry of irradiation and the beam quality resulted in a high level of reproducibility of the plasma conditions. The diagnostics used, namely, x-ray time-resolved spectroscopy and optical probing Nomarski interferometry, were both very successful and the experimental data are analyzed in detail. In particular two-dimensional density profiles have been provided whose quality, resolution, and extension are comparable with those obtained very recently in a test experiment using grid image refractometry [20]. The smearing of the fringe pattern in the dense region (observed in the early plasma expansion) can be strongly reduced in future experiments by using a shorter probe pulse.

The expansion dynamics of the plasma allows a variety of density profiles to be selected for interaction purposes, depending on the delay at which the interaction beam is set to reach the plasma. A few nanoseconds after formation, the plasma has 1-mm-sized blowoff at electron densities below $n_c/100$. This region is very suitable for studies of interaction phenomena in a low absorption regime. The peak density is well localized in a region whose size is comparable with the target diameter (0.4 mm). The peak-density region is separated from the low density blowoff by a gradient of 0.2–0.3 mm scale length along the axis of the interaction beam. A comparison with stimulated 1D expansion evidences a weak but clear confinement of the Al plasma by the plasma produced from the plastic substrate. This confinement, however, is limited to a small region close to the original target plane.

The amplitude of small scale (≈ 10 μm) inhomogeneities was estimated from the interferograms and resulted to be quite small making these plasmas very attractive for studies on laser-stimulated plasma instabilities. The plasma homogeneity was confirmed by the absence of second harmonic emission during plasma formation. The latter circumstance also provides an ideal condition of low background noise for second harmonic measurements during the interaction of a delayed beam with the preformed plasma.

The evolution of the electron temperature was measured during and after plasma formation using x-ray spectroscopy. Opacity effects on the x-ray line emission were taken in account and were found to be negligible at the time of interest for interaction studies. At 2 ns after the peak of the heating pulses the electron temperature was found to be 550 eV when the heating intensity on each side of the Al target was of 6×10^{13} W cm^{-2} and was estimated to be 400 eV at an intensity of 3×10^{13} W cm^{-2}. The maximum electron density at this time is expected to be approximately $0.1n_c$ in lower intensity case and $0.08n_c$ at the higher intensity.

In conclusion, a preformed plasma with a good transverse electron density homogeneity has been produced. The expansion fronts of the plasma are regular and it is predicted that, when irradiation takes place with an interaction beam focused in a spot of 100–200 μm with a large f/number, interaction will start with negligible perturbation by refraction effects. These features, together with the temperature of several hundreds of eV at the time of interest, make this kind of plasma extremely useful for studies devoted to a better understanding of the physics of the main instabilities affecting the corona of a laser irradiated ICF microsphere, including filamentation instability, stimulated Brillouin scattering, and stimulated Raman scattering.

ACKNOWLEDGMENTS

The authors greatly acknowledge the support of the Commission of the European Community under the Contract No. GE1-CT91-0034. The authors are very grateful to M. H. Key and the whole staff of the SERC Central Laser Facility for their invaluable and enthusiastic contribution to the experiment. The authors also acknowledge enlightening discussions with W. Seka.

APPENDIX

1. Abel inversion

The fringe pattern produced by the interferometer used in the experiment described here results from the interference between a laser beam which has propagated through the plasma and an unperturbed reference beam, both beams originating from the same laser source. According to the x,y,z reference frame shown in Fig. 1, the phase difference between these two beams in a given position (x,z) of an output plane perpendicular to the probe beam is given by

$$\Delta\varphi(x,z)=\frac{2\pi}{\lambda_p}\int_{-L/2}^{L/2}[\mu(x,y,z)-1]dy\ , \tag{A1}$$

where λ_p is the probe beam wavelength, μ is the plasma refractive index, and L is the total path length of the probe beam in the plasma, the plasma extent along y being smaller than L. Assuming that $n_e \ll n_c$, the plasma refraction index can be written as

$$\mu(x,y,z)\cong 1-\frac{n_e(x,y,z)}{2n_c}\ , \tag{A2}$$

where $n_e(x,y,z)$ is the plasma electron density and n_c is the critical density for the probe wavelength. The determination of $n_e(x,y,z)$ from the phase shift distribution is, in general, a very difficult task, unless the plasma has a cylindrical symmetry. Since in our experimental conditions both the target and the focal spots of each heating beam satisfy cylindrical symmetry around the x axis, we can expect the plasma itself to show the same symmetry, although minor deviations from the cylindrical symmetry might arise as heating beams are not normally incident on target. If the plasma has a cylindrical symmetry around the x axis, with the probe beam propagating along the y axis, Eq. (A1) can be rewritten in the form of the Abel integral equation to obtain $\mu(r,x)$. Assuming $n_e \ll n_c$, one finds the following expression for the electron density:

$$n_e(r,x)=-\frac{mc^2}{\pi e^2\lambda_p}\int_r^{r_0}\left[\frac{d\Delta\varphi(x,z)}{dz}\right]\frac{dz}{\sqrt{z^2-r^2}}\ , \qquad \text{(A3)}$$

where m and e are the electron mass and charge, respectively, c is the speed of light, r is the distance from the x axis, and r_0 is the radial plasma size.

2. Fourier transform method

The phase shift induced by the plasma is experimentally detected measuring the displacement of the fringes from their unperturbed position. The intensity of the fringe pattern on the film in presence of the plasma can be written as

$$I(x,z)=a(x,z)+[c(x,z)\exp(2\pi i f_u x)+\text{c.c.}]\ , \qquad \text{(A4)}$$

where $c(x,z)=\frac{1}{2}b(x,z)\exp[i\Delta\varphi(x,z)]$ and its complex conjugate $c^*(x,z)$ contain all the information relative to the phase shift induced by the plasma; $a(x,z)$ and $b(x,z)$ account for nonuniformities of the background intensity and the fringe visibility; f_u is the spatial frequency of the unperturbed fringe pattern, i.e., the number of fringes per unit length on the film; and $\Delta\varphi(x,z)$ is the phase shift induced by the plasma as given by Eq. (A1). According to the definition of logarithm of a complex number, one can write the following expression which relates the phase shift induced by the plasma to $c(x,z)$:

$$\ln[c(x,z)]=\ln[\tfrac{1}{2}b(x,z)]+i\Delta\varphi(x,z)\ . \qquad \text{(A5)}$$

The phase shift can therefore be obtained as the imaginary part of the complex logarithm of $c(x,z)$. In order to determine $c(x,z)$ from the experimental interferograms we take the Fourier transform of Eq. (A4) with respect to x:

$$F_I(f,z)=F_a(f,z)+F_c(f-f_u,z)+F_c^*(f+f_u,z)\ . \qquad \text{(A6)}$$

If the scale length of typical nonuniformities of the background intensity along x is large compared to the fringe separation, then the contribution of $F_c(f,z)$ in Eq. (A6), i.e., the Fourier transform of $c(x,z)$, will result well separated by the contribution due to the background intensity nonuniformities. In this case, we can extract $F_c(f-f_u,z)$ [or $F_c^*(f+f_u,z)$] from the Fourier spectrum, shift it by f_u toward the origin in order to obtain $F_c(f,z)$, and perform the inverse Fourier transform to obtain $c(x,z)$. According to Eq. (A5), the imaginary part of the complex logarithm of $c(x,z)$, i.e., the argument of $c(x,z)$, will finally give the phase distribution $\Delta\varphi(x,z)\pm 2n\pi$, n being an integer to be determined from the condition that the phase shift must be a continuous function. This last indetermination can be solved by setting an appropriate algorithm able to detect and compensate the jumps in the phase shift along both x and z take place.

The interferograms were digitized with the two scanning directions set along the x and z coordinates respectively, i.e., perpendicular and parallel to the unperturbed fringes (see Fig. 1). The optical density of the film was converted into intensity and stored in a two-dimensional array. A fast Fourier transform of the intensity distribution along the x direction was performed for each position on z axis.

[1] D. H. Phillion, E. M. Campbell, K. G. Estabrook, G. E. Phillips, and F. Ze, Phys. Rev. Lett. **49**, 1405 (1982).

[2] O. Willi, T. Afshar-rad, S. Coe, and A. Giulietti, Phys. Fluids B **2**, 1318 (1990).

[3] D. L. Matthews, P. L. Hagelstein, M. D. Rosen, M. J. Eckart, N. M. Ceglio, A. U. Hazi, H. Medecki, B. M. MacGowan, J. E. Trebes, B. L. Whitten, E. M. Campbell, C. W. Hatcher, A. M. Hawryluk, R. L. Kauffman, L. D. Pleasance, G. Rambach, J. H.Scofield, G. Stone, and T. A. Weaver, Phys. Rev. Lett. **54**, 110 (1985).

[4] R. A. London and M. D. Rosen, Phys. Fluids **29**, 3813 (1986).

[5] J. H. Hunter, Jr. and R. A. London, Phys. Fluids **31**, 3102 (1988).

[6] S. E. Coe, T. Afshar-rad, D. Bassett, J. Edwards, and O. Willi, Opt. Commun. **81**, 47 (1991).

[7] O. Willi, D. Bassett, A. Giulietti, and S. J. Karttunen, Opt. Commun. **70**, 487 (1989).

[8] S. E. Coe, T. Afshar-rad, and O. Willi, Opt. Commun. **73**, 299 (1989).

[9] C. Rousseaux, F. Amiranoff, C. Labaune, and G. Matthieussent, Phys. Fluids B **5**, 920 (1993).

[10] T. Afshar-rad, L. A. Gizzi, M. Desselberger, F. Khattak, O. Willi, and A. Giulietti, Phys. Rev. Lett. **68**, 942 (1992).

[11] W. Seka, R. E. Bahr, R. W. Short, A. Simon, R. S. Craxton, D. S. Montgomery, and A. E. Rubenchik, Phys. Fluids B **4**, 2232 (1992).

[12] S. H. Batha, D. D. Meyerhofer, A. Simon, and R. P. Drake, Phys. Fluids B **3**, 448 (1991).

[13] C. B. Darrow, R. P. Drake, D. S. Montgomery, P. E. Young, K. Estabrook, W. L. Kruer, and T. W. Johnston, Phys. Fluids B **3**, 1473 (1991).

[14] W. Seka, R. S. Craxton, R. E. Bahr, D. L. Bradley, P. A. Jaanimagi, B. Yaakobi, and R. Epstein, Phys. Fluids B **4**, 432 (1992).

[15] A. Giulietti, T. Afshar-Rad, V. Biancalana, P. Chessa, C. Danson, D. Giulietti, L. A. Gizzi, E. Schifano, S. M. Viana, and O. Willi, RAL Report No. RAL-93-031, 1993 (un-

published), p. 38.
[16] V. Biancalana and P. Chessa, Appl. Opt. (to be published).
[17] M. G. Nomarski, Phys. Rad. **16**, 95 (1955).
[18] R. Benattar, C. Popovics, and R. Siegel, Rev. Sci. Instrum. **50**, 1583 (1979).
[19] O. Willi, in *Laser-Plasma Interaction 4,* Proceedings of XXXV SUSSP, St. Andrews, 1988, edited by M. B. Hooper (SUSSP, Edinburgh, 1989).
[20] R. S. Craxton, F. S. Tuner, R. Hoefen, C. Darrow, E. F. Gabl, and Gar. E. Bush, Phys. Fluids B **5**, 4419 (1993).
[21] I. H. Hutchinson, *Principles of Plasma Diagnostics* (Cambridge University Press, London, 1987).
[22] M. Takeda, H. Ia, and S. Kobayashi, J. Opt. Soc. Am. **72**, 156 (1982).
[23] K. A. Nugent, Appl. Opt. **18**, 3101 (1985).
[24] A. Giulietti, D. Giulietti, D. Batani, V. Biancalana, L. Gizzi, L. Nocera, and E. Schifano, Phys. Rev. Lett. **63**, 524 (1989).
[25] R. W. Lee, L. Whitten, and R. E. Stout II, J. Quant. Spectrosc. Radiat. Transfer **32**, 91 (1984).
[26] G. Bekefi, *Principles of Laser Plasmas* (Wiley, New York, 1976).
[27] J. P. Christiansen, D. E. Ashby, and K. V. Roberts, Comput. Phys. Commun. **7**, 271 (1974).
[28] P. A. Rodgers, A. M. Rogoyski, and S. J. Rose, RAL Report No. RAL-89-127, 1989 (unpublished).
[29] L. Spitzer, Jr. and R. Härm, Phys. Rev. **89**, 977 (1953).
[30] R. C. Malone, R. L. McCrory, and R. L. Morse, Phys. Rev. Lett. **34**, 721 (1975).
[31] O. Willi, D. S. Tabatabaei, D. Riley, H. Hauer, N. Delamater, C. Chenais-Popovics, P. Apte, and A. Cole, Phys. Rev. A **39**, 6090 (1989).
[32] E. M. Epperlein, Phys. Rev. Lett. **65**, 2145 (1990).
[33] R. L. Berger, B. F. Lasinski, T. B. Kaiser, E. A. Williams, A. B. Langdon, and B. I. Cohen, Phys. Fluids B **5**, 2243 (1993).
[34] M. H. Key, in *Handbook of Plasma Physics,* edited by M. N. Rosenbluth and R. Z. Sagdeev (North-Holland, Amsterdam, 1991), Vol. III, p. 593.
[35] M. Desselberger, T. Afshar-rad, F. Kattak, S. Viana, and O. Willi, Phys. Rev. Lett. **68**, 1539 (1992).

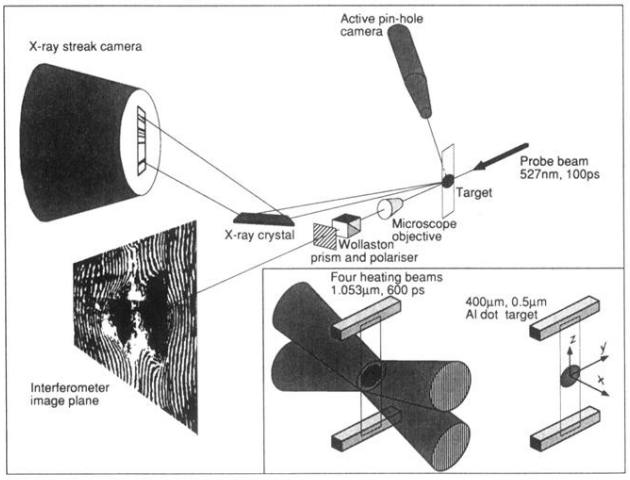

FIG. 1. Experimental setup for the production and characterization of long scale length expanding plasmas for ICF coronal studies. In the separate frame enclosed in the figure also represented are the Al dot target, the plastic substrate and the target holder (right), and the configuration of the four heating beams on target.

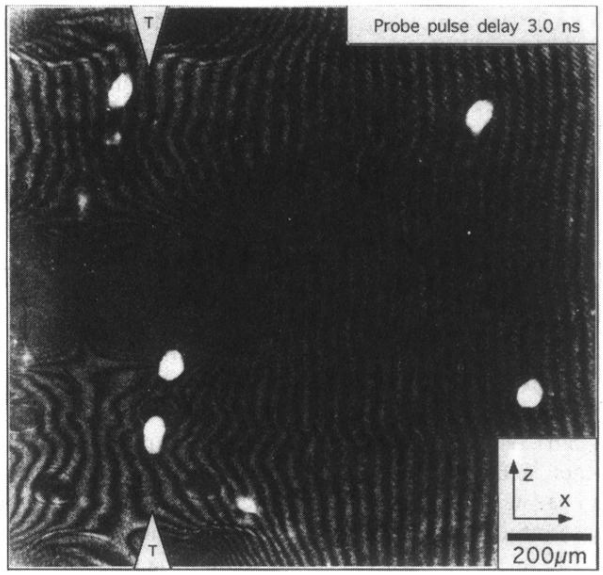

(a)

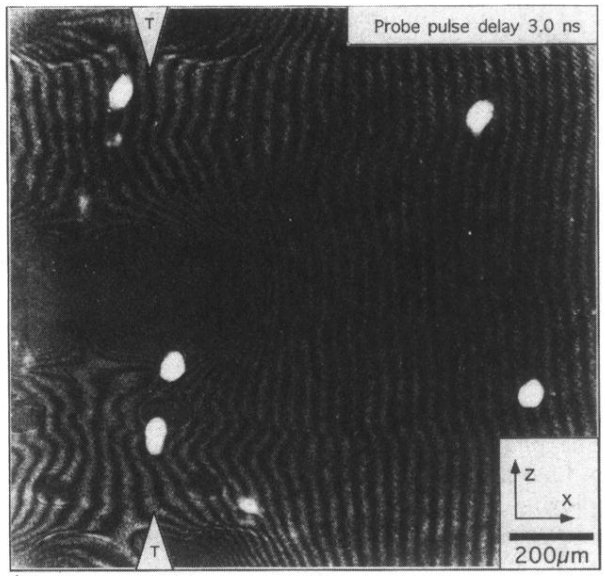

(b)

FIG. 2. (a) Interferogram of the preformed plasma taken 4.3 ns after the peak of the heating laser pulses. The intensity on target was 8.5×10^{13} W/cm^2. The probe pulse length was 100 ps and the probe wavelength was 0.53 μm. The original target position is shown by the arrows labeled with a T. (b) Interferogram of the preformed plasma taken 3.0 ns after the peak of the heating laser pulses. The intensity on target was 6.0×10^{13} W/cm^2. Other features are the same as in (a).

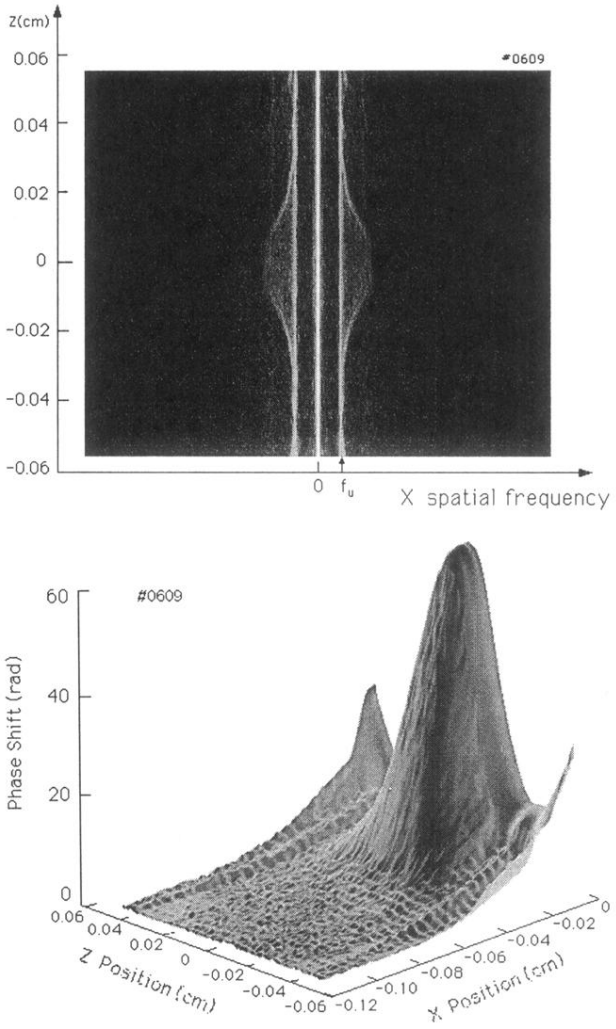

FIG. 3. Top: fast Fourier transform (FFT) of the intensity profile of the interferogram of Fig. 2(a). The FFT was performed along the x axis, perpendicular to the unperturbed fringes. The natural logarithm of the modulus of the FFT is shown as a grey-scale image. Bottom: 3D shaded surface of the phase shift distribution as obtained from the interferogram of Fig. 2(a) using a Fourier transform based technique (see text).

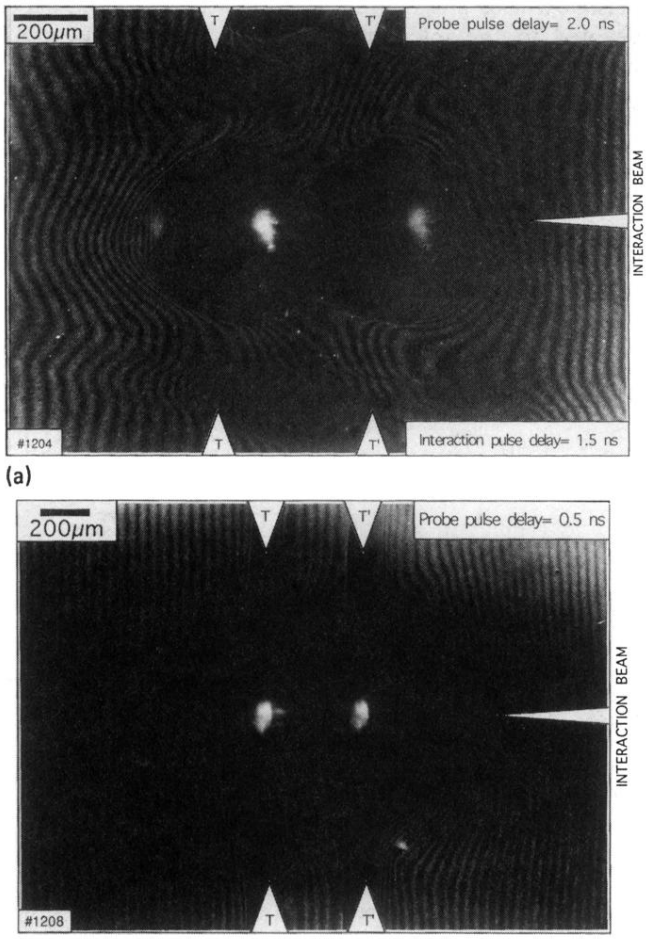

FIG. 7. (a) Interferogram of the preformed plasma taken 2.0 ns after the peak of the heating pulses showing the SH emitted by the interaction beam (heating to interaction delay: 1.5 ns). The total heating intensity was 9.4×10^{13} W/cm^2 while the interaction intensity was 1.2×10^{13} W/cm^2. (b) Interferogram of the plasma produced by a localized heating of the dot aluminum target showing strong SH emission in proximity of the target surface. Probe pulse delay 0.5 ns.

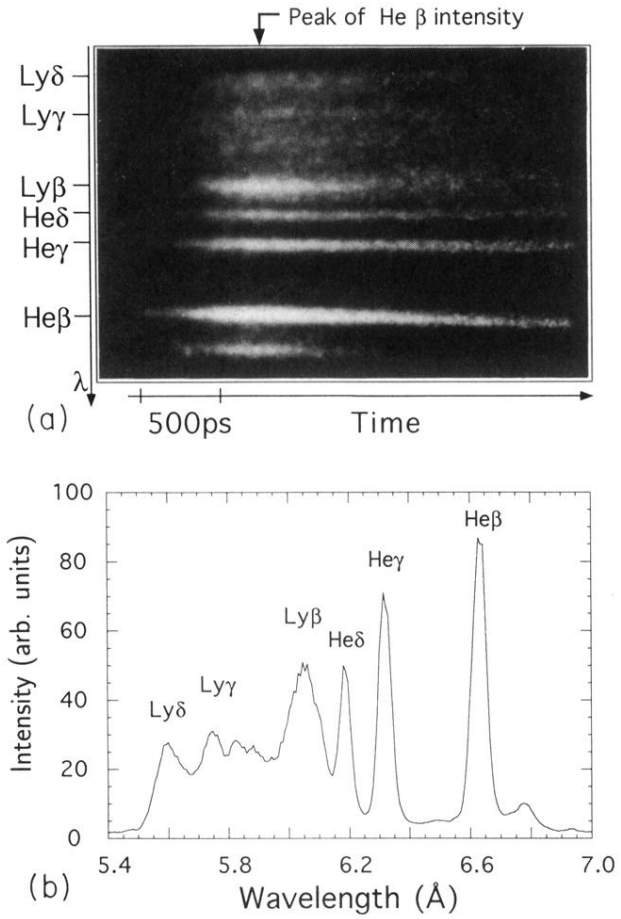

FIG. 8. (a) Time-resolved x-ray spectrum of *K*-shell Al emission from plasma produced at a heating intensity of 6×10^{13} W/cm^2. (b) Line out of the spectrum of (a) taken 500 ps after the peak of He β line intensity and integrated over 50 ps, which is the temporal resolution of the spectrum.

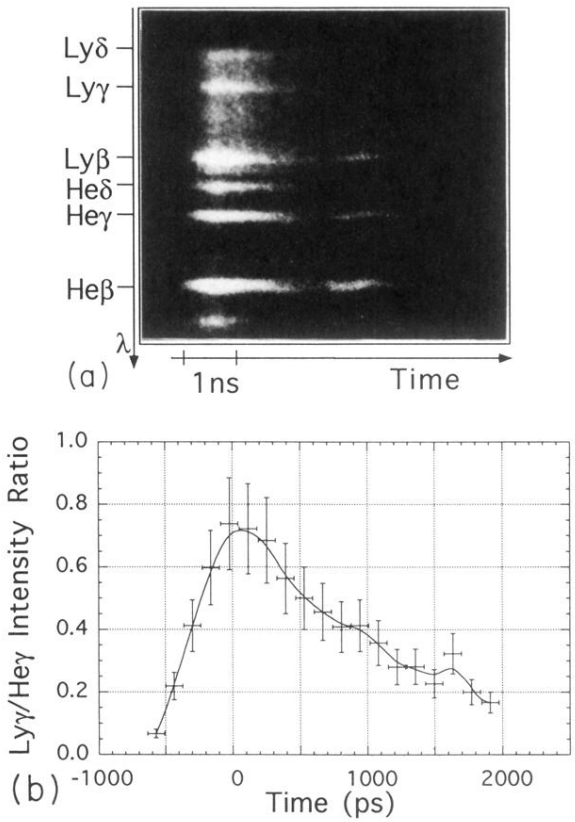

FIG. 9. (a) Time-resolved x-ray spectrum of K-shell Al emission from plasma produced at a heating intensity of 1.2×10^{14} W/cm^2. In this case the interaction beam was delayed by 2.5 ns with respect to the peak of the heating pulses. (b) Experimental intensity ratio of the H-like Al γ line ($1s$-$4p$) to the He-like Al γ line ($1s^2$-$1s4p$) as a function of time relative to the peak emission.